A Novel Control Scheme of Three-Phase Single-Switch Quasi-CRM Boost Rectifier

Kai Yao, *Member, IEEE*, Qingsai Meng, Fei Yang, *Member, IEEE*, and Siwen Yang

***Abstract*—A three phase single switch boost rectifier, operating in a quasi-critical conduction mode of the inductor current, can achieve the power factor correction and meet the IEC 61000-3-2. However, the switching frequency is variable in a line cycle, and the design of the inductor and electromagnetic interference filter as well as the power component selection is deteriorated. In this paper, a novel constant frequency control method is proposed for the converter by modulating the on-time of the switch. Compared with the traditional variable frequency control, the proposed control scheme achieves a constant switching frequency in a line cycle, which simplifies the design of the power devices, especially the magnetic components. Furthermore, the switching frequency and the rms value of the inductor current are also reduced, which contributes to a higher efficiency.**

***Index Terms*—Constant frequency control (CFC), rectifier, quasi-critical conduction mode (QCRM), variable frequency control (VFC).**

I. Introduction

IN ORDER to reduce the input current harmonics and its influence on the grid, rectifiers with power factor correction (PFC) are necessary for three phase ac–dc power conversion applications [1]. Many topologies and control strategies have been presented and discussed, where single switch, dual switches, three switches, four switches, and six switches are adopted, respectively [2]–[4]. With the number of the switch increasing, the power factor (PF) is improved at the expense of the control complexity and the cost [5]–[7]. For cost-sensitive applications of a low and medium power level, the single-switch converter is a good choice for its simple construction, easy control, and low cost [8].

Normally, a three-phase single-switch boost rectifier works in a discontinuous conduction mode (DCM) or a quasi-critical conduction mode (QCRM) [9]–[12]. DCM has the characteristics of an acceptable PF, a constant switching frequency, and a simple control [9]–[10]. Compared to constant duty cycle control, the optimal utilization control of switching cycles by modulating the duty cycle of a three-phase single-switch DCM boost rectifier for the efficiency improvement is proposed in [13], and the PF improvement method is put forward in [14]. In comparison with DCM, QCRM features a higher PF, a variable switching frequency, and a little more complex control [11], [12]. In addition, the switching frequency is dependent on the load and the input voltage. At a light load, the increase of the switching frequency results in a high switching loss, and the large variable frequency range complicates the inductor design, device selection, and electromagnetic interference (EMI) filter design [15]–[17].

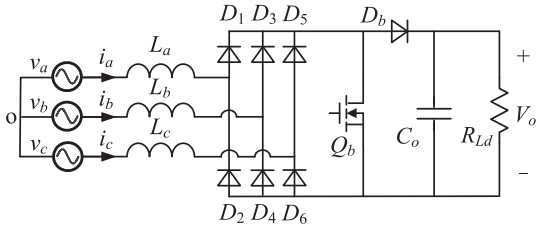

Fig. 1. Main circuit of three-phase single-switch boost rectifier.

A novel constant frequency control (CFC) strategy of the three-phase single switch boost rectifier is proposed in this paper. Compared with traditional variable frequency control (VFC), CFC achieves constant frequency in a line cycle that will simplify the design of EMI filter and inductor. In addition, the efficiency of the converter with CFC is improved, compared to that with VFC. In Section II, the operating principle of a QCRM three-phase single switch boost rectifier is studied. In Section III, the CFC scheme and the implementation circuit are put forward. Section IV deals with the comparison between CFC and VFC in terms of the power factor and the input current harmonics, the inductor current ripple, and the output voltage ripple. A 3 kW prototype has been built and tested, and the experimental results are presented in Section V.

II. Working Mechanism of Three-Phase Single-Switch Boost Rectifier

The main circuit of a three-phase single-switch boost rectifier is shown in Fig. 1, where $L_a = L_b = L_c = L$.

The three phase input voltage is defined as

$$v_a = V_m \sin \omega t \tag{1}$$

$$v_b = V_m \sin(\omega t - 2\pi/3) \tag{2}$$

$$v_c = V_m \sin(\omega t + 2\pi/3) \tag{3}$$

Manuscript received June 7, 2016; revised September 15, 2016; accepted October 11, 2016. Date of publication October 26, 2016; date of current version March 24, 2017. This work was supported in part by the National Natural Science Foundation of China under Grants 51307085 and 51677091, in part by the Excellent Youth Fund Project of Jiangsu Natural Science Foundation under Grant BK20160086, and in part by the Six Talents Peak Project of Jiangsu Province under Grant XNY-033. Recommended for publication by Associate Editor R. Redl.

The authors are with the School of Automation, Nanjing University of Science and Technology, Nanjing 210094, China (e-mail: yaokai@njust.edu.cn; zzmengsai@163.com; carryyangs@gmail.com; 314414414@qq.com).

Color versions of one or more of the figures in this paper are available online at http://ieeexplore.ieee.org.

Digital Object Identifier 10.1109/TPEL.2016.2621417

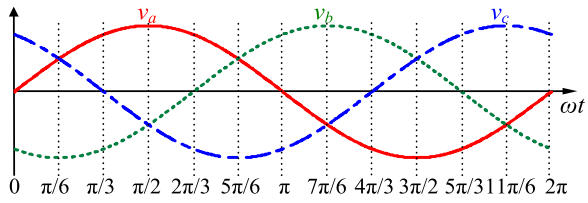

Fig. 2. Three-phase input voltage waveforms.

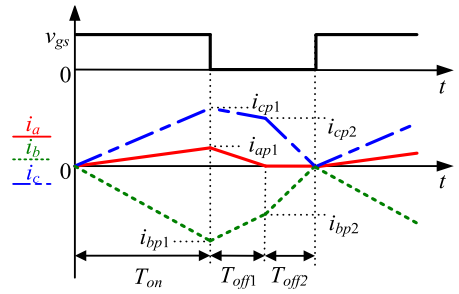

Fig. 3. Inductor current waveforms in a switching cycle during [0, π/6].

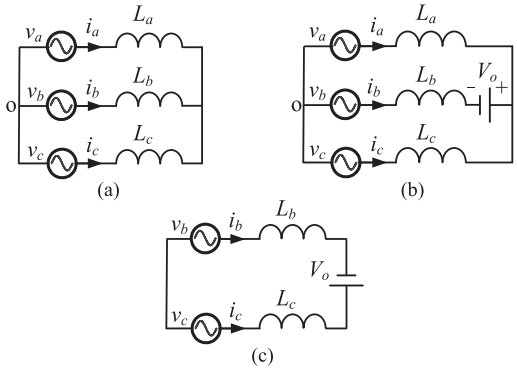

Fig. 4. (a) Q_b conducts; (b) Q_b turns OFF; (c) Q_b turns OFF and $i_a = 0$.

where ω and V_m are respectively the angular frequency and amplitude of the input voltage.

For a three phase balanced system

$$v_a + v_b + v_c = 0 \tag{4}$$

$$i_a + i_b + i_c = 0. \tag{5}$$

Fig. 2 is the waveform of the three phase input voltage. Each section of π/6 can be obtained by fractionizing an input cycle into 12 parts. The relationship between the polarity and relative amplitude of the three-phase voltage is constant in each section. During a switching cycle within [0, π/6], the waveform of the inductor current is shown in Fig. 3.

1) Operation condition 1: When Q_b is ON, D_1, D_5, and D_4 conduct. The simplified circuit is shown in Fig. 4(a), from which we have

$$v_a - Ldi_a/dt = v_b - Ldi_b/dt = v_c - Ldi_c/dt. \tag{6}$$

According to (4)–(6), we can obtain the rising rate of the inductor current as

$$\begin{aligned} di_a/dt &= v_a/L \\ di_b/dt &= v_b/L \\ di_c/dt &= v_c/L. \end{aligned} \tag{7}$$

When Q_b turns OFF, the inductor current of each phase achieves its peak value as

$$i_{\mathrm{ap1}} = T_{\mathrm{on}} \cdot di_a/dt = \frac{v_a}{L} T_{\mathrm{on}} \tag{8a}$$

$$i_{\mathrm{bp1}} = T_{\mathrm{on}} \cdot di_b/dt = \frac{v_b}{L} T_{\mathrm{on}} \tag{8b}$$

$$i_{\mathrm{cp1}} = T_{\mathrm{on}} \cdot di_c/dt = \frac{v_c}{L} T_{\mathrm{on}} \tag{8c}$$

where T_{on} is the on time.

2) Operation condition 2: When Q_b is OFF, D_b conducts. The simplified circuit is shown in Fig. 4(b), from which we can see that

$$v_a - v_b - V_o = L\left(di_a/dt - di_b/dt\right) \tag{9a}$$

$$v_c - v_b - V_o = L\left(di_c/dt - di_b/dt\right) \tag{9b}$$

where V_o is the output voltage.

According to (4), (5), and (9), the falling rate of the inductor current is

$$di_a/dt = \left(v_a - V_o/3\right)/L \tag{10a}$$

$$di_b/dt = \left(v_b + 2V_0/3\right)/L \tag{10b}$$

$$di_c/dt = \left(v_c - V_0/3\right)/L. \tag{10c}$$

When i_a falls to zero first, the corresponding time of this period is

$$T_{\mathrm{off1}} = \frac{i_{\mathrm{ap1}}}{|di_a/dt|} = \frac{3v_a}{V_o - 3v_a} T_{\mathrm{on}}. \tag{11}$$

When i_a reaches zero, i_b and i_c are

$$i_{\mathrm{bp2}} = i_{\mathrm{bp1}} + \frac{di_b}{dt} T_{\mathrm{off1}} = \frac{V_o\left(v_b + 2v_a\right)}{V_o - 3v_a} \frac{T_{\mathrm{on}}}{L} \tag{12a}$$

$$i_{\mathrm{cp2}} = -i_{\mathrm{bp2}} = -\frac{V_o\left(v_b + 2v_a\right)}{V_o - 3v_a} \frac{T_{\mathrm{on}}}{L}. \tag{12b}$$

3) Operation condition 3: When i_a is zero, the simplified circuit is shown in Fig. 4(c), from which we have

$$v_c - v_b - V_o = L\left(di_c/dt - di_b/dt\right) \tag{13a}$$

$$i_b = -i_c. \tag{13b}$$

According to (13), the falling rate of the inductor current is

$$di_b/dt = -di_c/dt = \left(V_o + v_b - v_c\right)/2L. \tag{14}$$

Based on (12) and (14), the relevant falling time interval of i_b and i_c is

$$T_{\mathrm{off2}} = \frac{|i_{\mathrm{bp2}}|}{|di_b/dt|} = \frac{2V_o\left(v_b + 2v_a\right)}{\left(V_o + v_b - v_c\right)\left(3v_a - V_o\right)} T_{\mathrm{on}}. \tag{15}$$

From (11) and (15), the switching cycle is

$$T_s = T_{\mathrm{on}} + T_{\mathrm{off1}} + T_{\mathrm{off2}} = \frac{V_o}{\left(V_o + v_b - v_c\right)} T_{\mathrm{on}}. \tag{16}$$

The switching frequency can be expressed as

$$f_s = \frac{1}{T_s} = \frac{V_o + v_b - v_c}{V_o T_{\mathrm{on}}}. \tag{17}$$

Similar with the analysis of [0, π/6], the switching frequency during other periods can be derived as

$$f_s = \begin{cases} \dfrac{V_o + v_b - v_c}{V_o T_{\rm on}} = \dfrac{V_o - v_g}{V_o T_{\rm on}} & (0 \le \omega t \le \pi/6) \\ \dfrac{V_o + v_b - v_a}{V_o T_{\rm on}} = \dfrac{V_o - v_g}{V_o T_{\rm on}} & (\pi/6 \le \omega t \le \pi/3) \\ \dfrac{V_o + v_b - v_a}{V_o T_{\rm on}} = \dfrac{V_o - v_g}{V_o T_{\rm on}} & (\pi/3 \le \omega t \le \pi/2) \\ \dfrac{V_o + v_c - v_a}{V_o T_{\rm on}} = \dfrac{V_o - v_g}{V_o T_{\rm on}} & (\pi/2 \le \omega t \le 2\pi/3) \\ \dfrac{V_o + v_c - v_a}{V_o T_{\rm on}} = \dfrac{V_o - v_g}{V_o T_{\rm on}} & (2\pi/3 \le \omega t \le 5\pi/6) \\ \dfrac{V_o + v_c - v_b}{V_o T_{\rm on}} = \dfrac{V_o - v_g}{V_o T_{\rm on}} & (5\pi/6 \le \omega t \le \pi) \end{cases} . \tag{18}$$

According to Fig. 3, the average value of the inductor current during a switching cycle within [0, π/6] can be deduced as

$$i_{a\_ave} = \frac{(T_{\rm on} + T_{\rm off1})}{T} \frac{i_{ap1}}{2} = I_0 \frac{M \sin \omega t - \frac{1}{2} \sin 2\omega t}{M - \sqrt{3} \sin \omega t} \tag{19a}$$

$$\begin{aligned} i_{b\_ave} &= \frac{1}{2T} \left[T_{\rm on} i_{\rm bp1} + T_{\rm off1} \left(i_{\rm bp1} + i_{\rm bp2} \right) + T_{\rm off2} i_{\rm bp2} \right] \\ &= I_0 \frac{M \sin \left(\omega t - \frac{2\pi}{3} \right) + \sin 2\omega t}{M - \sqrt{3} \sin \omega t} \end{aligned} \tag{19b}$$

$$\begin{aligned} i_{c\_ave} &= \frac{1}{2T} \left[T_{\rm on} i_{\rm cp1} + T_{\rm off1} \left(i_{\rm cp1} + i_{\rm cp2} \right) + T_{\rm off2} i_{\rm cp2} \right] \\ &= I_0 \frac{M \sin \left(\omega t + \frac{2\pi}{3} \right) - \frac{1}{2} \sin 2\omega t}{M - \sqrt{3} \sin \omega t} \end{aligned} \tag{19c}$$

where $I_0 = V_m T_{\rm on}/(2L)$ and $M = V_0/(\sqrt{3} V_m)$

Similar analyses can be adopted to other sections of [π/6, π], and the average input current of Phase a, i.e., the average inductor current within [0, π], is

$$\begin{aligned} i_{{\rm in}\_a} &= i_{a\_{\rm ave}} \\ &= I_0 k_n \left(\omega t \right) \left(\frac{n-1}{6} \pi \le \omega t \le \frac{n}{6} \pi n = 1, 2, \ldots, 6 \right) \end{aligned} \tag{20}$$

where

$$k_1 \left(\omega t \right) = \frac{M \sin \omega t - \frac{1}{2} \sin 2\omega t}{M - \sqrt{3} \sin \omega t} \tag{21a}$$

$$k_2 \left(\omega t \right) = \frac{M \sin \omega t + \frac{1}{2} \sin 2 \left(\omega t + \frac{2\pi}{3} \right)}{M - \sqrt{3} \sin \left(\omega t + \frac{2\pi}{3} \right)} \tag{21b}$$

$$k_3 \left(\omega t \right) = \frac{M \sin \omega t - \sin 2 \left(\omega t + \frac{2\pi}{3} \right)}{M + \sqrt{3} \sin \left(\omega t + \frac{2\pi}{3} \right)} \tag{21c}$$

$$k_4 \left(\omega t \right) = \frac{M \sin \omega t + \sin 2 \left(\omega t - \frac{2\pi}{3} \right)}{M + \sqrt{3} \sin \left(\omega t - \frac{2\pi}{3} \right)} \tag{21d}$$

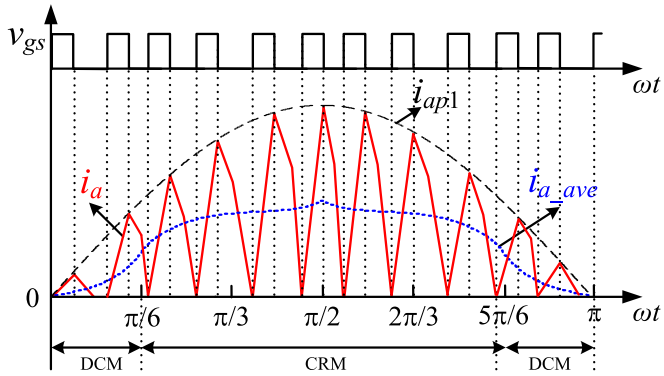

Fig. 5. Inductor current waveform in a half line cycle.

$$k_5 \left(\omega t \right) = \frac{M \sin \omega t - \frac{1}{2} \sin 2 \left(\omega t - \frac{2\pi}{3} \right)}{M - \sqrt{3} \sin \left(\omega t - \frac{2\pi}{3} \right)} \tag{21e}$$

$$k_6 \left(\omega t \right) = \frac{M \sin \omega t + \frac{1}{2} \sin 2\omega t}{M - \sqrt{3} \sin \omega t}. \tag{21f}$$

Based on the above analysis, the instantaneous waveform, the average value and the peak value of i_a can be drawn in Fig. 5.

III. Control Scheme of Constant Switching Frequency QCRM

A. Proposition of the CFC Scheme

According to (18), if

$$T_{\rm on} \left(t \right) = \alpha \frac{V_o - v_g}{V_o}, \tag{22}$$

then the switching frequency f_s will be

$$f_s = \frac{1}{\alpha}. \tag{23}$$

Substituting (22) into (20), the expression of the input current can be obtained as

$$i_{{\rm in}\_a} = \alpha \frac{V_m}{2L} \frac{V_o - v_g}{V_o} k_n \left(\omega t \right). \tag{24}$$

Supposing that the efficiency is 100%, according to (1) and (24), the expression of the average input power of Phase a can be calculated as

$$\begin{aligned} P_{{\rm in}\_a} &= \frac{4}{T_{\rm line}} \int_0^{\frac{T_{\rm line}}{4}} v_a i_{{\rm in}\_a} dt \\ &= \alpha \frac{V_m^2}{\pi L} \sum_{n=1}^{3} \int_{\frac{(n-1)\pi}{6}}^{\frac{n\pi}{6}} \frac{V_o - v_g}{V_o} k_n \left(\omega t \right) \sin \omega t d\omega t \\ &= \alpha \frac{V_m^2}{\pi L} h \left(M \right) = \frac{P_o}{3} \end{aligned} \tag{25}$$

where $h(M) = \sum_{n=1}^{3} \int_{\frac{(n-1)\pi}{6}}^{\frac{n\pi}{6}} \frac{V_o - v_g}{V_o} k_n \left(\omega t \right) \sin \omega t d\omega t$.

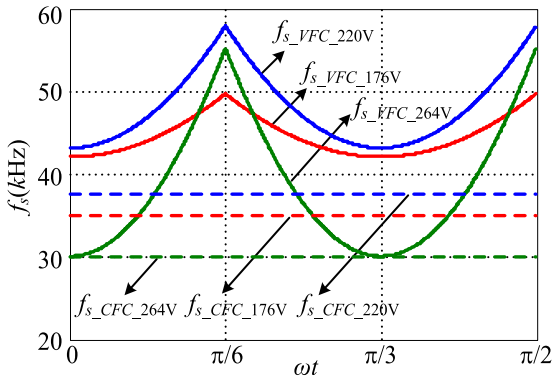

Fig. 6. Curves of switching frequency during [0, π/2].

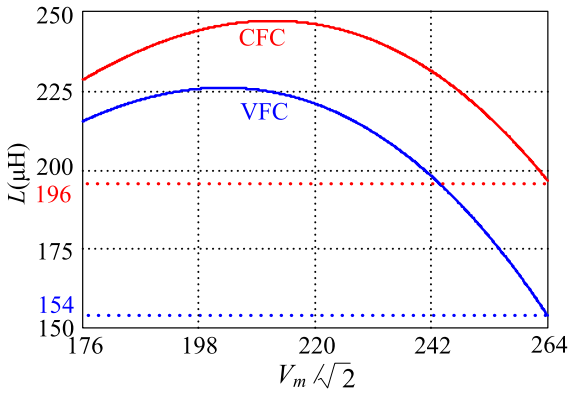

Fig. 7. Critical inductance over phase voltage range.

From (22), (23), and (25), $T_{\rm on}$, and f_s can be obtained as

$$T_{\rm on}\left(t\right) = \frac{\pi L P_o}{3V_m^2 h\left(M\right)} \frac{V_o - v_g}{V_o} \tag{26a}$$

$$f_s = \frac{3V_m^2 h\left(M\right)}{\pi L P_o}. \tag{26b}$$

When the parameters of the converter are certain, (26) shows that f_s is constant. In this way, the constant frequency QCRM is obtained.

B. Derivation of Inductance

From (1) and (20), the average value of the input power of phase *a* can be calculated as

$$\begin{aligned} P_{\text{in\_}a} &= \frac{4}{T_{\rm line}} \int_0^{\frac{T_{\rm line}}{4}} v_a i_{\text{in\_}a} dt \\ &= \frac{2I_0 V_m}{\pi} \sum_{n=1}^{3} \int_{\frac{(n-1)\pi}{6}}^{\frac{n\pi}{6}} k_n\left(\omega t\right) \sin \omega t d\omega t \\ &= \frac{2I_0 V_m}{\pi} j\left(M\right) = \frac{P_o}{3} \end{aligned} \tag{27}$$

where $j(M) = \sum_{n=1}^{3} \int_{\frac{(n-1)\pi}{6}}^{\frac{n\pi}{6}} k_n(\omega t) \sin \omega t d\omega t$.

For VFC, $T_{\rm on}$ is obtained from (27) as

$$T_{\rm on} = \frac{\pi L P_o}{3V_m^2 j\left(M\right)}. \tag{28}$$

For VFC, the switching frequency is variable. In combination with the parameters of the converter given in Section V, f_s during [0, π/2] at the inputs of 176, 220, and 264 V are depicted based on (18) and (28), respectively, as shown in Fig. 6. It can be seen that f_s gets its minimum at $\omega t = 0$ and $\omega t = \pi/3$, and its maximum at $\omega t = \pi/6$, which can be expressed as

$$f_{s\_\text{VFC}\_\min} = \frac{3V_m^2\left(V_o - \sqrt{3}V_m\right)}{\pi L P_o V_o} j\left(M\right) \tag{29a}$$

$$f_{s\_\text{VFC}\_\max} = \frac{3V_m^2\left(V_o - \frac{3}{2}V_m\right)}{\pi L P_o V_o} j\left(M\right). \tag{29b}$$

From (23) and (26), f_s with CFC can be expressed as

$$f_{s\_\text{CFC}} = \frac{1}{\alpha} = \frac{3V_m^2}{\pi L P_o} h\left(M\right). \tag{30}$$

To prevent the switching noise from falling into the human hearing range, the designed minimum switching frequency $f_{s\_\min} = 30$ kHz. From (29a), the inductance with VFC can be obtained as

$$L_1 \le \frac{3V_m^2\left(V_o - \sqrt{3}V_m\right)}{\pi P_o V_o f_{S\_\min}} j\left(M\right). \tag{31}$$

From (30), the inductance with CFC is obtained as

$$L_2 \le \frac{3V_m^2}{\pi P_o f_{S\_\min}} h\left(M\right). \tag{32}$$

According to (31), (32), and the parameters of the converter, the critical inductance in the two control methods can be figured out as shown in Fig. 7. In order to ensure $f_s \ge 30$ kHz, the critical inductances of VFC and CFC are 154 and 196 μH, respectively.

C. Control Circuit

Fig. 8 shows the control circuit of the proposed CFC scheme. The rectified voltage is sensed by a differential sampler, and $v_A = mv_g$, where m is the sampling coefficient. The output voltage is detected by R_8 and R_9 with the same gain, i.e., $v_B = mV_o$. When $R_{10} = R_{11} = R_{12} = R_{13}$, the output of the subtractor will be $v_C = v_B - v_A = m(V_o - v_g)$. The output voltage is regulated by an error amplifier, and the sensed output voltage across a voltage divider composed of R_{14} and R_{15} is compared with the reference voltage $V_{\rm ref}$, given the condition that $V_{\rm ref}$ is set as 2.5 V, and the output voltage sense gain is set at 2.5/750, i.e., $R_{15}/(R_{14} + R_{15}) = 1/1300$.

v_B, v_C and the error signal $v_{\rm EA}$ are sent to the multiplier, and

$$v_{\rm Ton} = v_{\rm EA\_CFC} \frac{m\left(V_o - v_g\right)}{mV_o} = v_{\rm EA\_CFC}\left(1 - \frac{v_g}{V_o}\right). \tag{33}$$

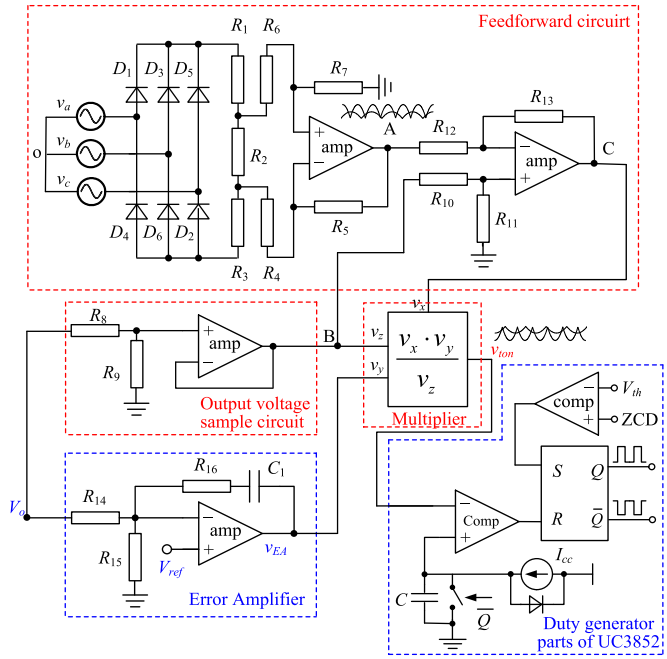

Fig. 8. Control circuit.

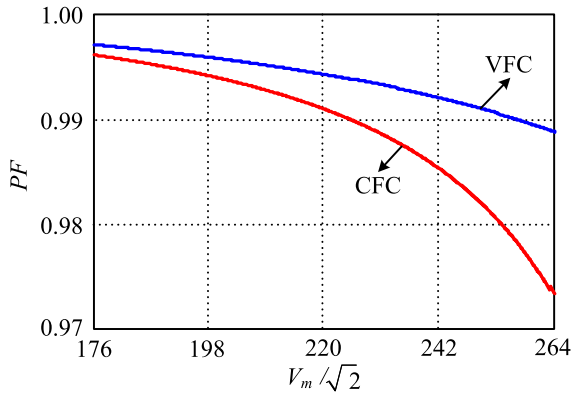

Fig. 9. Comparison of input PF.

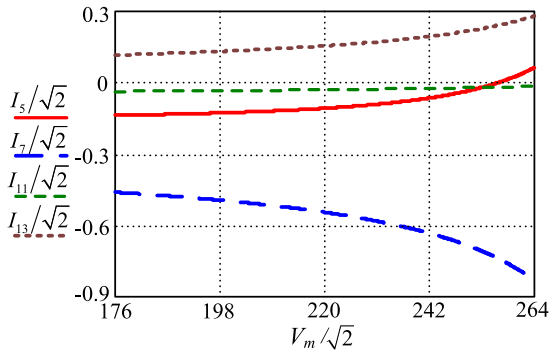

Fig. 10. RMS value of the 5th, 7th, 11th, and 13th harmonics.

IV. Performance Comparison

A. Input Power Factor and Harmonics

Taking (28) into (20), and (26) into (24), the average input current with VFC and CFC can be calculated as

$$i_{\text{in\_}a\text{\_VFC}} = \frac{\pi P_o k_n(\omega t)}{6V_m j(M)} \tag{34}$$

$$i_{\text{in\_}a\text{\_CFC}} = \frac{\pi P_o k_n(\omega t)\frac{V_o - v_g}{V_o}}{6V_m h(M)} \tag{35}$$

where $(n-1)\pi/6 \le \omega t \le n\pi/6 n = 1, 2, \ldots, 6$.

From (1), (34), and (35), the PF with VFC and CFC are

$$\begin{aligned}\text{PF\_VFC} &= \frac{P_{\text{in\_}a}}{\frac{V_m}{\sqrt{2}} I_{a\_\text{rms}}} \\ &= \frac{\frac{2}{\pi}\int_0^{\frac{\pi}{2}} v_a i_{\text{in\_}a} d\omega t}{\frac{V_m}{\sqrt{2}}\sqrt{\frac{2}{\pi}\int_0^{\frac{\pi}{2}} i_{\text{in\_}a}^2 d\omega t}} = \frac{\frac{2}{\sqrt{\pi}} j(M)}{\sqrt{s(M)}}\end{aligned} \tag{36a}$$

$$\begin{aligned}\text{PF\_CFC} &= \frac{P_{\text{in\_}a}}{\frac{V_m}{\sqrt{2}} I_{a\_\text{rms}}} \\ &= \frac{\frac{2}{\pi}\int_0^{\frac{\pi}{2}} v_a i_{\text{in\_}a} d\omega t}{\frac{V_m}{\sqrt{2}}\sqrt{\frac{2}{\pi}\int_0^{\frac{\pi}{2}} i_{\text{in\_}a}^2 d\omega t}} = \frac{\frac{2}{\sqrt{\pi}} h(M)}{\sqrt{u(M)}}\end{aligned} \tag{36b}$$

where $s(M) = \sum_{n=1}^{3} \int_{\frac{(n-1)\pi}{6}}^{\frac{n\pi}{6}} k_n^2(\omega t) d\omega t$ and $u(M) = \sum_{n=1}^{3} \int_{\frac{(n-1)\pi}{6}}^{\frac{n\pi}{6}} \left(\frac{V_o - v_g}{V_o} k_n(\omega t)\right)^2 d\omega t$.

According to (36), Fig. 9 is figured out. Comparing with VFC, there is a little sacrifice in PF with CFC, especially at a high input voltage. However, in most cases operating at the normal voltage of 220 V, the converter still achieves a high PF more than 0.99 with CFC.

In order to show the harmonics, Fourier analysis is adopted on the input current

$$I_n = \frac{1}{\pi}\int_0^{2\pi} i_{\text{in\_}a} \cdot \sin(n\omega t) d\omega t \quad (n = 1, 2, 3 \ldots). \tag{37}$$

Substituting (34) and (35) into (37), we could get the input current harmonics with VFC and CFC.

Fig. 10 presents the curves of input current harmonics with CFC. According to IEC 61000-3-2 Class A, the rms values of the 5th, 7th, 11th, and 13th harmonics should be lower than 1.2, 0.77, 0.33, and 0.21 A, respectively. It can be seen that the 5th and 11th harmonics with CFC satisfy the requirement; however, the 7th and 13th harmonics exceed the limit when the input voltage is around 264 VAC. For the rated input voltage of 220 V, all the harmonics meet the standard.

B. Inductor Current Ripple

From the analyses of Section II, the expressions of i_a, i_b and i_c during a switching cycle within [0, π/6] can be obtained. As the inductor current is in phase with the input voltage, the rms value of the inductor current of phase a during [π/6, π/3] and [π/3, π/2] equals that of phase c and phase b during [0, π/6]

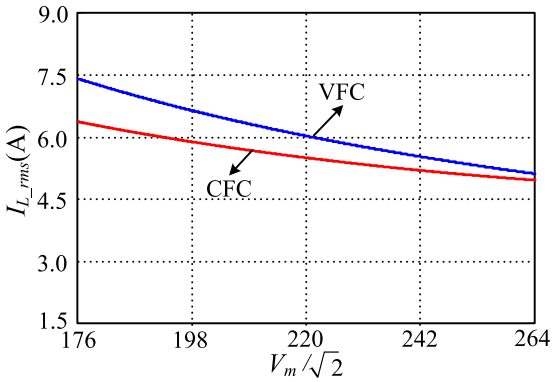

Fig. 11. RMS value of boost inductor current.

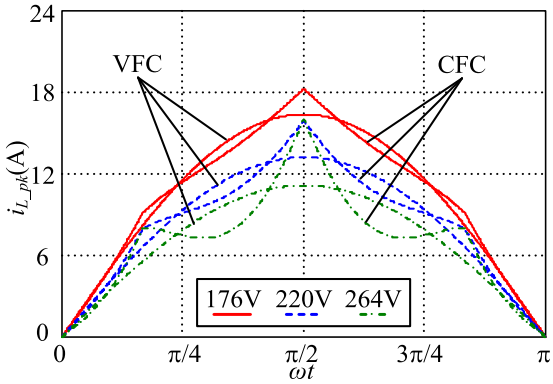

Fig. 12. Peak value of inductor current.

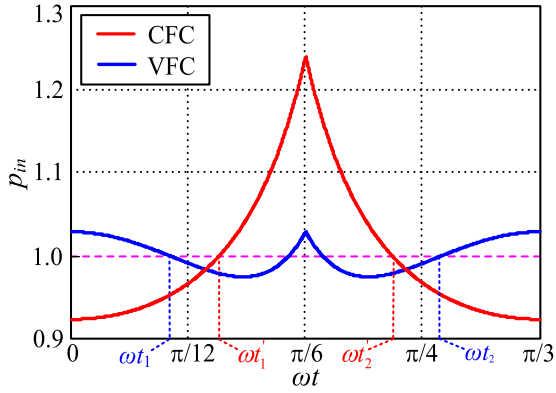

Fig. 13. Normalized instantaneous input power.

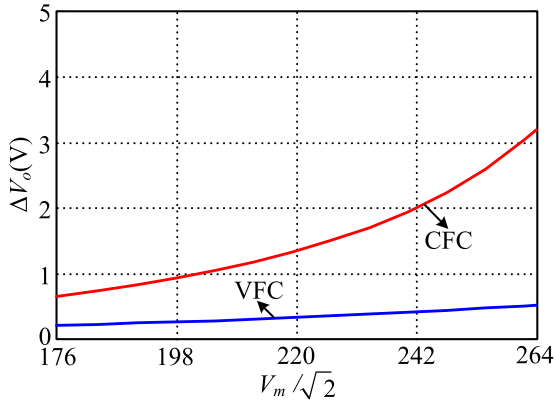

Fig. 14. Output voltage ripple.

respectively. Therefore, the rms value of the inductor current in a line cycle is

$$I_{L\_\mathrm{rms}} = \sqrt{\frac{2}{\pi}\int_0^{\frac{\pi}{6}} \left[\frac{1}{T_s}\int_0^{T_s} (i_a^2 + i_b^2 + i_c^2)dt\right] d\omega t}. \quad (38)$$

According to (1)–(3), (11), and (15), substituting (28) with $L_1 = 230\ \mu$H as well as (22) and (26) with $L_2 = 294\ \mu$H into (38), respectively, and in combination with the parameters of the converter, I_{L_rms} with both control schemes can be acquired and shown in Fig. 11. It can be seen that I_{L_rms} is almost the same.

Substituting (28) with $L_1 = 230\ \mu$H, (22) and (26) with $L_2 = 294\ \mu$H into (8), the peak value of the inductor current with both control schemes can be calculated, respectively, as shown in Fig. 12. Comparing with VFC, the peak value of the inductor current of the converter with CFC increases at around $\pi/6$, $\pi/2$, and $5\pi/6$, and decreases at around $\pi/3$ and $2\pi/3$.

C. Output Voltage Ripple

Phases *a*, *b*, and *c* all feature a difference of $2\pi/3$ sequentially, and so does the corresponding input current. According to (34) and (35), i_{in_b} and i_{in_c} can be deduced. Then, the normalized instantaneous input power with respect to the output power can be obtained as

$$p_{\mathrm{in}}^* = \left(v_a i_{\mathrm{in}\_a} + v_b i_{\mathrm{in}\_b} + v_c i_{\mathrm{in}\_c}\right)/P_0. \quad (39)$$

According to (39), p_{in1}^* and p_{in2}^* for VFC and CFC are calculated and shown in Fig. 13 respectively during [0, $\pi/3$] at 220 V input.

Although p_{in}^*>1, the storage capacitor C_o is charged, otherwise discharged. The output voltage ripple can be derived as

$$\Delta V_{o1} = \left[2P_o\int_0^{t_1}(p_{\mathrm{in1}}^* - 1)\,dt\right]/C_0V_0 \quad (40a)$$

$$\Delta V_{o2} = \left[2P_o\int_0^{t_1'}(1 - p_{\mathrm{in2}}^*)\,dt\right]/C_0V_0. \quad (40b)$$

Based on (39) and (40), Fig. 14 is plotted, which shows that the ripple of the output voltage with CFC is higher than that with VFC.

V. Experimental Verification

In order to validate the aforementioned analysis, a prototype has been made and tested in the lab. The main parameters are: v_{in} = 176-264 VAC/50 Hz; V_o = 750 VDC; P_o = 3 kW; $f_{s\,\mathrm{in}}$ = 30 kHz.

Figs. 15 and 16 show the full load experimental waveforms of the input voltage, input current, boost inductor current, and output voltage ripple with VFC and CFC at 176, 220, and 264 VAC input, respectively. It can be seen that with both of the control schemes, due to QCRM, the input current is not sinusoidal. A

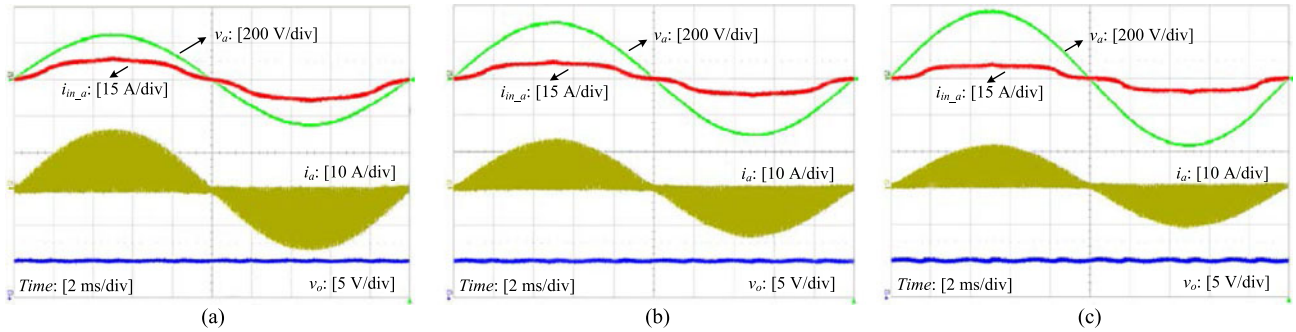

Fig. 15. Experimental waveforms of input voltage, input current, inductor current, and output voltage with VFC at 100% load. (a) 176 VAC, (b) 220 VAC, and (c) 264 VAC.

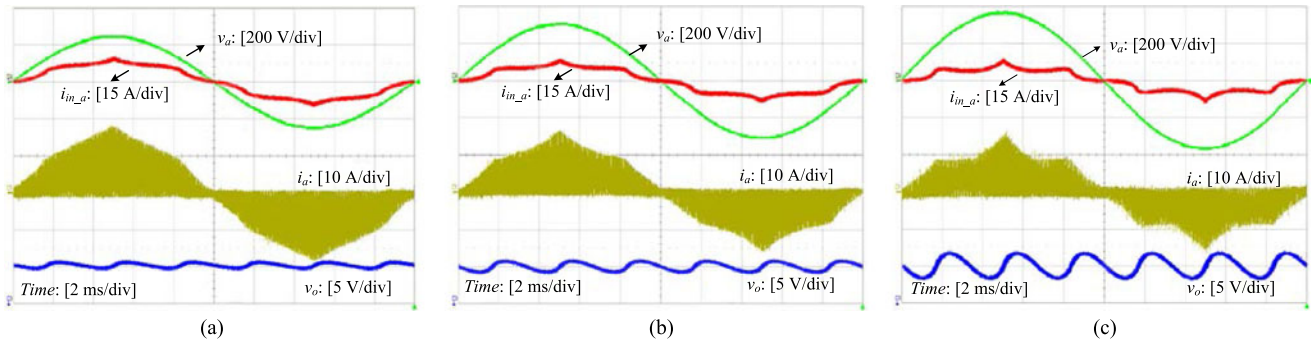

Fig. 16. Experimental waveforms of input voltage, input current, inductor current, and output voltage with CFC at 100% load. (a) 176 VAC, (b) 220 VAC, and (c) 264 VAC.

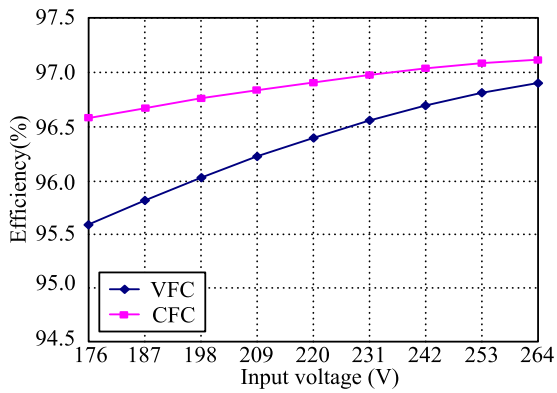

Fig. 17. Measured efficiency.

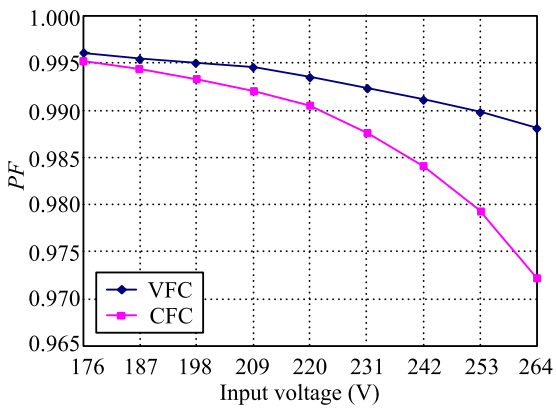

Fig. 18. Measured PF.

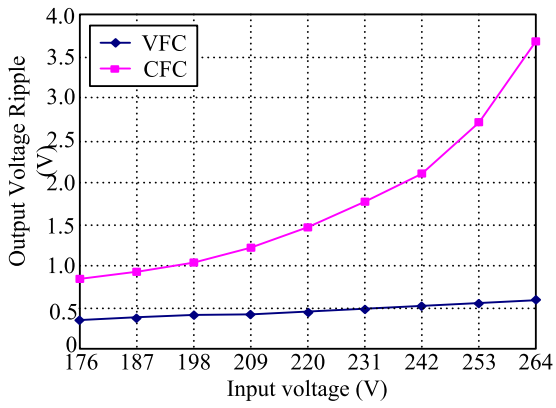

Fig. 19. Measured output voltage ripple.

larger input voltage means more severe distortion. The shape of the input current and the inductor current is the same as the theoretical analysis.

Figs. 17–19 show the full load experimental curves of the measured efficiency, PF, and output voltage ripple, respectively.

From Fig. 17, it can be seen that the efficiency of the converter with CFC is higher than that with VFC, particularly at low line voltage. The reason is as follows. From Fig. 11, it can be seen that the rms value of the inductor current with CFC has a slight reduction compared to that with VFC, which will decrease the conduction loss. Furthermore, in Fig. 12, at a low input voltage, the peak value of the inductor current, i.e., the peak value of the switch current, increases at around $\pi/6$, $\pi/2$, and $5\pi/6$ and decreases at other angles, and most important of all, the

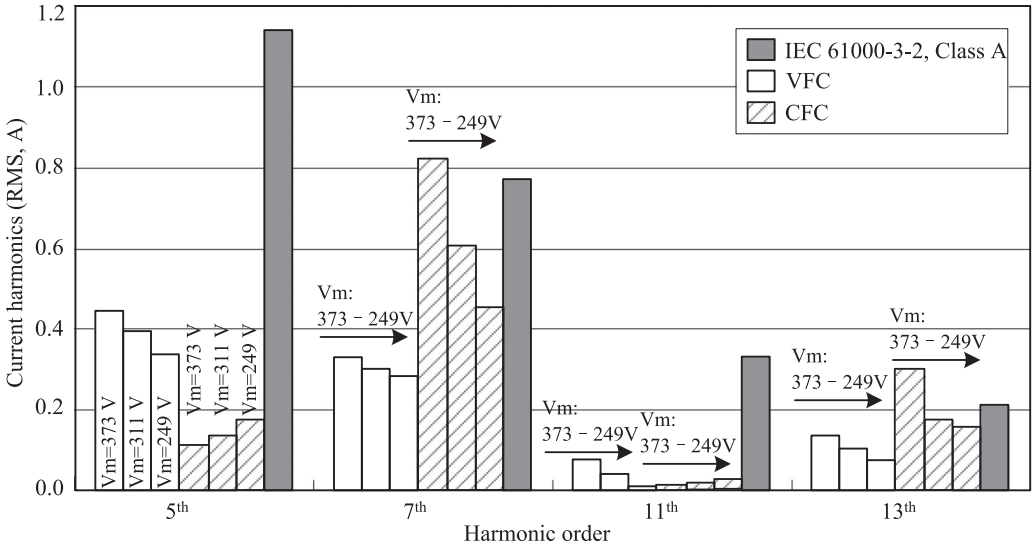

Fig. 20. Measured input current harmonics.

switching frequency is greatly reduced, as shown in Fig. 6. Therefore, the switching turn-off loss is reduced. Furthermore, the rectifier diode loss, the boost inductor loss, and the output capacitor loss are reduced as well.

According to Fig. 18, CFC achieves the PF which is lower than that with VFC. A larger input voltage results in a lower PF. The measured results agree well with that of the theoretical analysis shown in Fig. 9.

As seen from Fig. 19, the output voltage ripple of the converter with CFC is higher than that with VFC. The output voltage ripple becomes higher with the increasing input voltage. The measured result is in conformity with that of the theoretical analysis shown in Fig. 14.

Fig. 20 shows the measured 5th, 7th, 11th, and 13th harmonics of the input current at 100% load, where for CFC, compared to that for VFC, the 5th and 11th harmonics reduce, whereas the 7th and 13th harmonics increase. The measurement is consistent with the theoretical analysis shown in Fig. 10.

VI. Conclusion

When the three-phase single switch QCRM boost rectifier operates with constant on-time of the switch control method, although the input power factor is relatively high, the switching frequency is variable during a line cycle, which goes against the design of inductor and EMI filter. Therefore, a constant switching frequency QCRM operation is proposed, as well as the variation rule of the on-time and the control circuit. Furthermore, the PF, the input current harmonics, the inductor current ripple, and the output voltage ripple are analyzed in detail. The results show that the efficiency of the converter with the CFC is higher than that with the VFC, while the contrary is the case as for the power factor and the output voltage ripple.

References

[1] O. Garcia, J. A. Cobos, R. Prieto, P. Alou, and J. Uceda, "Power factor correction: A survey," *IEEE Trans. Ind. Electron.*, vol. 18, no. 3, pp. 749–755, May 2003.

[2] A. Bouafia, F. Krim, and J. Gaubert, "Fuzzy-logic-based switching state selection for direct power control of three-phase PWM rectifier," *IEEE Trans. Ind. Electron.*, vol. 56, no. 6, pp. 1984–1992, Jun. 2009.

[3] N. Vázquez, H. Rodriguez, C. Hernández, E. Rodríguez, and J. Arau, "Three-phase rectifier with active current injection and high efficiency," *IEEE Trans. Ind. Electron.*, vol. 56, no. 1, pp. 110–119, Jan. 2009.

[4] A. Gensior, H. Sira-Ramírez, J. Rudolph, and H. Guldner, "On some nonlinear current controllers for three-phase boost rectifiers," *IEEE Trans. Ind. Electron.*, vol. 56, no. 2, pp. 360–370, Feb. 2009.

[5] J. W. Kolar and T. Friedli, "The essence of three-phase PFC rectifier systems—Part I," *IEEE Trans. Power Electron.*, vol. 28, no. 1, pp. 176–198, Jan. 2013.

[6] T. Friedli, M. Hartmann, and J. W. Kolar, "The essence of three-phase PFC rectifier systems—Part II," *IEEE Trans. Power Electron.*, vol. 29, no. 2, pp. 543–560, Feb. 2014.

[7] A. R. Prasad, P. D. Ziogas, and S. Manias, "An active power factor correction technique for three-phase diode rectifiers," *IEEE Trans. Power Electron.*, vol. 6, no. 1, pp. 83–92, Jan. 1991.

[8] Y. Jang and M. M. Jovanović, "A comparative study of single-switch three-phase high-power-factor rectifiers," *IEEE Trans. Ind. Electron.*, vol. 34, no. 6, pp. 1327–1334, Nov./Dec. 1998.

[9] J. W. Kolar, H. Ertl, and F. C. Zach, "Space vector-based analytical analysis of the input current distortion of a three-phase discontinuous-mode boost rectifier system," *IEEE Trans. Power Electron.*, vol. 10, no. 6, pp. 733–745, Nov. 1995.

[10] Y. Jang and M. M. Jovanović, "A novel robust harmonic injection method for single-switch three-phase discontinuous- conduction-mode boost rectifiers," *IEEE Trans. Power Electron.*, vol. 13, no. 5, pp. 824–834, Sep. 1998.

[11] K. Cai and Z. Xu, "A novel control method of three-phase single-switch Boost power factor corrector under variable switching frequency," in *Proc. Int. Conf. Power Syst. Technol.*, 2002, pp. 565–569.

[12] L. Simonetti, J. Sebastian, and J. Uceda, "Single-switch three-phase power factor under variable switching frequency and discontinuous input current," in *Proc. IEEE Power Electron. Spec. Conf.*, Seattle, USA, 1993, pp. 657–662.

[13] K. Yao, Q. Meng, Y. Bo, and W. Hu, "Three-phase single-switch DCM boost PFC converter with optimum utilization control of switching cycles," *IEEE Trans. Ind. Electron.*, vol. 63, no. 1, pp. 60–70, Jan. 2016.

[14] K. Yao, X. Ruan, C. Zou, and Z. Ye, "Three-phase single-switch boost power factor correction converter with high input power factor," *IET Power Electron.*, vol. 5, no. 7, pp. 1095–1103, 2012.

[15] V. Vlatkovic, D. Borojevic, and F. C. Lee, "Input filter design for power factor correction circuits," *IEEE Trans. Power Electron.*, vol. 11, no. 1, pp. 199–205, Jan. 1996.

[16] Y. Jang and R. W. Erickson, "New single-switch three-phase high power factor rectifiers using multi-resonant zero current switching," *IEEE Trans. Power Electron.*, vol. 13, no. 1, pp. 194–201, Jan. 1998.

[17] T. Yan, J. Xu, F. Zhang, J. Sha, and Z. Dong, "Variable-on-time-controlled critical-conduction-mode flyback PFC converter," *IEEE Trans. Ind. Electron.*, vol. 61, no. 11, pp. 6091–6099, Nov. 2014.

Kai Yao (M'14) was born in Jiangsu Province, China, in 1980. He received the B.S. degree in industrial automation from Nantong University, Nantong, China, in 2002, the M.S. degree in mechanical design and theory and the Ph.D. degree in electrical engineering from Nanjing University of Aeronautics and Astronautics, Nanjing, China, in 2005 and 2010, respectively.

In 2011, he joined the Faculty of Electrical Engineering, School of Automation, Nanjing University of Science and Technology, where he has been engaged in teaching and research in the field of power electronics. His research interests include power factor correction converters, renewable energy generation system, and power supplies for LED.

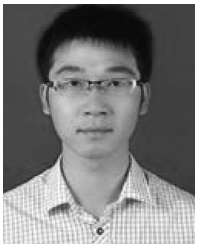

Qingsai Meng was born in Henan Province, China, in 1991. He received the B.S. degree in electrical engineering from Zhengzhou University of Light Industry, Zhengzhou, China, in 2013. He is currently working toward the M.S. degree in power electronics at Nanjing University of Science and Technology, Nanjing, China.

His research interests include power factor correction converters.

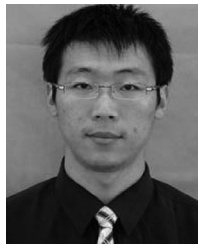

Fei Yang (M'16) was born in Shanxi, China, in 1983. He received the B.S. and Ph.D. degrees in electrical engineering from the Nanjing University of Aeronautics and Astronautics, Nanjing, China, in 2006 and 2013, respectively.

From February 2014 to September 2015, he worked as a Postdoctoral Researcher in the Department of Mechanical Engineering, Katholieke Universiteit Leuven, Leuven, Belgium. In October 2015, he joined the Faculty of Electrical Engineering, School of Automation, Nanjing University of Science and Technology, Nanjing, China, where he has been involved in teaching and research in the field of power electronics. His research interests include power factor correction converters, electromagnetic interference filter design, dc/dc converters, and pulse power generator for micro-EDM.

Dr. Yang has been a Reviewer of the IEEE TRANSACTIONS ON INDUSTRIAL ELECTRONICS and the IEEE TRANSACTIONS ON POWER ELECTRONICS since 2014 and 2011, respectively.

Siwen Yang was born in Fujian Province, China, in 1992. He received the B.S. degree in electrical engineering and automation from Jiangsu University, Zhenjiang, China, in 2015. He is currently working toward the M.S. degree in power electronics at Nanjing University of Science and Technology, Nanjing, China.

His research interests include power factor correction converters.